New insights into particle detection with superheated liquids

2011 New J. Phys. 13 043006

(http://iopscience.iop.org/1367-2630/13/4/043006)

New Journal of Physics
The open-access journal for physics

New insights into particle detection with superheated liquids

S Archambault[1,9], F Aubin[1,9], M Auger[1,10], M Beleshi[2], E Behnke[3], J Behnke[3], B Beltran[4], K Clark[5,11], X Dai[5,12], M Das[6], A Davour[5], F Debris[1], J Farine[2], M-H Genest[1,13], G Giroux[1,10], R Gornea[1,10], R Faust[1], H Hinnefeld[3], A Kamaha[5], C Krauss[4], M Lafrenière[1], M Laurin[1], I Lawson[7], C Leroy[1], C Lévy[5,14], L Lessard[1], I Levine[3], J-P Martin[1], S Kumaratunga[1], R MacDonald[4], P Nadeau[2,15], A Noble[5], M-C Piro[1], S Pospisil[8], N Starinski[1], I Stekl[8], N Vander Werf[3], U Wichoski[2] and V Zacek [1,16] (The PICASSO Collaboration)

[1] Département de Physique, Université de Montréal, Montréal, H3C 3J7, Canada
[2] Department of Physics, Laurentian University, Sudbury, P3E 2C6, Canada
[3] Department of Physics and Astronomy, Indiana University South Bend, South Bend, IN 46634, USA
[4] Department of Physics, University of Alberta, Edmonton, T6G 2G7, Canada
[5] Department of Physics, Queens University, Kingston, K7L 3NG, Canada
[6] Center for AstroParticle Physics, Saha Institute for Nuclear Physics, Kolkata 700 064, India
[7] SNOLAB, 1039 Regional Road 24, Lively, P3Y 1N2, Canada
[8] Institute of Experimental and Applied Physics, Czech Technical University in Prague, Prague, Cz-12800, Czech Republic
E-mail: zacekv@lps.umontreal

New Journal of Physics **13** (2011) 043006 (25pp)
Received 18 November 2010
Published 7 April 2011
Online at http://www.njp.org/
doi:10.1088/1367-2630/13/4/043006

[9] Present address: Department of Physics, McGill University, Montréal, H3A 2T8, Canada.
[10] Present address: Laboratorium für Hochernergiephysik, Universität Bern, CH-3012 Bern, Switzerland.
[11] Present address: Department of Physics, University of Oxford, Oxford OX1 3PU, UK.
[12] Present address: AECL Chalk River Laboratories, Chalk River, ON, K0J 1J0, Canada.
[13] Present address: Fakultät für Physik, Ludwig-Maximilians-Universität, D-85748 Garching, Germany.
[14] Present address: Physik Department, Universität Münster, D-48149 Münster, Germany.
[15] Present address: Department of Physics, Queens University, Kingston, K7L 3NG, Canada.

Abstract. We report new results obtained from calibrations of superheated liquid droplet detectors used in dark matter searches with different radiation sources (n, α, γ). In particular, detectors were spiked with α-emitters located inside and outside the droplets. It is shown that the responses have different temperature thresholds, depending on whether α-particles or recoil nuclei create the signals. The measured temperature threshold for recoiling ^{210}Pb nuclei from ^{214}Po α-decays was found to be in agreement with test beam measurements using mono-energetic neutrons. A comparison of the threshold data with theoretical predictions shows deviations, especially at high temperatures. It is shown that signals produced simultaneously by recoil nuclei and α-particles have more acoustic energy than signals produced by one or the other separately. A model is presented that describes how the observed intensities of particle-induced acoustic signals can be related to the dynamics of bubble growth in superheated liquids. A growth scenario that is limited by the inertia of the surrounding liquid shows a trend that is supported by the data. An improved understanding of the bubble dynamics is an important first step in obtaining better discrimination between particle types interacting in detectors of this kind.

Contents

[16] Author to whom any correspondence should be addressed.

1. Introduction

The PICASSO dark matter experiment uses the superheated droplet technique, which is based on the operation principle of the classic bubble chamber [1]–[5]. Detectors of this kind are threshold devices, where the operating parameters (pressure and temperature) determine the energy threshold. Since each temperature, at a given pressure, corresponds to a defined recoil energy threshold, the spectrum of the particle-induced energy depositions can be reconstructed in superheated liquids by measuring the rate as a function of temperature.

In the case of PICASSO, the active detector liquid is dispersed as droplets of a metastable superheated perfluorobutane, C_4F_{10}, and the detectors are operated in a temperature range such that nuclear recoils in the keV range induced by interactions with weakly interacting particles (WIMPS) could trigger bubble formation. These explosive evaporations are accompanied by acoustic signals, which are recorded by piezoelectric transducers. Operating these detectors at sufficiently low temperatures and still being fully sensitive to eventual WIMP-induced nuclear recoils makes them almost entirely unaffected by backgrounds due to recoiling electrons and minimum ionizing radiation. The only remaining particle-induced background (other than neutrons) is α-particles. In previous studies the PICASSO collaboration showed that the acoustic signals contain information about the nature of the primary event [6]–[8]: it was observed that the acoustic signals produced by α-emitters are more intense than the signals of neutron- or WIMP-induced recoil events. Recently, this effect was confirmed by the COUPP and SIMPLE collaborations, which used it for a substantial background reduction in their dark matter searches [9, 10].

The underlying physics process can be explained by the hypothesis that, in the case of α-emitters, the recoiling nucleus and the extended α-track contribute at least two vapourization centres to the total signal, whereas the signals of the considerably more localized nuclear recoils carry the imprint of one single nucleation only. In the following, we describe recent efforts aimed at consolidating this hypothesis and determining potential paths to improved particle-type discrimination.

This paper is organized as follows. In section 2, we give an overview of the detection principle and the underlying theoretical model proposed by Seitz [11], which still serves as the reference theory to describe the radiation sensitivity of superheated liquids. Section 3 describes the current generation of PICASSO detectors for dark matter searches and their piezoelectric read-out. Calibration measurements with detectors spiked with α-emitters of known types and energies (^{241}Am and ^{226}Ra) are discussed in section 4. In these tests, the α-emitters were deliberately located outside and inside the droplets. The results, together with data obtained from existing detectors containing relatively large contaminations with α-emitters, show that, as expected, mono-energetic nuclear recoils from α-decays are detected at lower temperatures than α-particles. These observations are then compared in section 5 with the results from test beam measurements using mono-energetic neutrons with energies between 4.8 keV and 4 MeV, and they are found to be in good agreement. Section 6 presents the data for γ-ray-induced nucleations which also fit the described model well. The effect of an intrinsic energy resolution defining the temperature thresholds of the α and neutron responses is discussed in section 7. Since the energy depositions per unit path length of nuclear recoils are larger than the energy deposition by the Bragg peak of the α-particles themselves, the latter information can be used, as described in section 8, to infer a more precise estimate of the so-called nucleation parameter b. This is an empirical parameter in the Seitz model, which describes the spatial extension of

the energy deposition necessary for creating a nucleation. Section 9 discusses the intensities of acoustic signals produced by neutrons, α-emitters and γ-rays. Signals of α-emitters located within droplets are produced simultaneously by recoil nuclei and α-particles and are shown to be more intense than signals produced by one or the other separately, or in particular by WIMP-induced recoils. Finally, in section 10, a plausible argument is presented to explain the observed α-recoil discrimination in terms of the dynamics of bubble growth in superheated liquids. This is largely uncharted terrain; nevertheless some conclusions can be drawn that shed light on the early phase of particle-induced bubble formation.

2. Detection principle and theoretical model

For a phase transition to occur in a superheated liquid the prevailing theoretical model proposed by Seitz [11] predicts that a critical minimum amount of energy E_c has to be supplied within a local thermal spike and if the resulting proto-bubble reaches a volume of critical radius R_c, it becomes thermodynamically unstable and grows rapidly. Thermodynamics predicts that the growth of the bubble passes through several stages of acceleration and deceleration, which also gives rise to a detectable pressure wave (section 10).

Both R_c and E_c decrease exponentially with temperature and are given by

$$R_c(T) = \frac{2\sigma}{\Delta p}, \tag{1}$$

$$E_c(T) = -\frac{4\pi}{3} R_c^3 \Delta p + \frac{4\pi}{3} R_c^3 \rho_v h_{lv} + 4\pi R_c^2 \left(\sigma - T\frac{d\sigma}{dT}\right) + W_{irr}, \tag{2}$$

where σ is the surface tension at the liquid–vapour interface, $\Delta p = p_v - p_e$ is the degree of superheat, which is the difference between the vapour pressure p_v and the external pressure p_e, ρ_v is the density of the gas phase, and h_{lv} is the latent heat of evaporation. All of these quantities depend on the temperature of operation T. The first term in expression (2) is the reversible, mechanical work W_m done during expansion to a bubble of size R_c against the pressure of the liquid (and is negative for a superheated bubble). The second term represents the energy W_{ev} needed to evaporate the liquid as the bubble grows to critical size. The third term describes the work W_{lv} initially needed to create the liquid–vapour interface of the protobubble. W_{irr} is the work which goes into irreversible processes, such as acoustic wave emission; this contribution is small compared with the others.

Radiation-induced phase transitions imply that the locally deposited kinetic energy of a traversing particle exceeds the critical energy, i.e. $E_{dep} \geqslant E_c(T)$ and that the stopping power of the particle is large enough to supply this energy as heat over a distance L_c such that it is effective in reaching the critical energy within a protobubble of critical size R_c [12]:

$$E_{dep}(T) = \int_0^{L_c(T)} \frac{dE}{dx}\, dx \geqslant E_c(T). \tag{3}$$

Experimentally, relatively good agreement is reported between E_{dep} and E_c for several halocarbons and for energies around $E_c = 17$ keV and larger [13]. The situation is different for L_c, where a large range of values is quoted. Since R_c is the natural length scale of the process, L_c is usually given in terms of $L_c = bR_c$, where b varies from author to author: $L_c = 2R_c$ appears to be intuitively justified and is supported by data for low-energy thresholds below $E_c = 20$ keV;

Table 1. Predictions by the Seitz model for $E_c(T)$ and $R_c(T)$ in C_4F_{10} using relations (1) and (2) and the values for ρ_v, h_{fg}, σ and p_v compiled by NIST [20]. Also quoted are the ranges $R_{F,C}$ for fluorine and carbon ions with kinetic energies corresponding to the given values of E_c.

T (°C)	E_c (keV)	R_c (nm)	R_F (nm)	R_C (nm)
10	1000	280	2540	3600
20	111.1	111	590	1090
30	27.8	60	99	210
40	7.45	35.3	20	40

$L_c = 2\pi R_c = 6.28 R_c$ is proposed in [14] following arguments of the stability of vapour jets in liquids, whereas some authors propose $L_c = (\rho_v/\rho_l)^{1/3} R_c \approx 6.6 R_c$, where ρ_l and ρ_v are the densities of the liquid and vapour phases, respectively. Furthermore, a temperature dependence of the nucleation parameter was reported with b values increasing up to 20 and larger for thresholds for neutron-induced recoils above 1 MeV [12]–[19]. As described in section 8, our recent results from calibration measurements with mono-energetic neutrons and α-emitters in PICASSO shed additional light on this issue.

The active detector material in PICASSO, C_4F_{10}, has a boiling temperature of $T_b = -1.7\,°C$ at a pressure of 1.013 bar and a critical temperature of $T_c = 113.3\,°C$; therefore at ambient temperature and pressure this liquid is in a metastable, superheated state. Table 1 summarizes the predictions of the Seitz model for $E_c(T)$ and $R_c(T)$ using relations (1) and (2) and the values for ρ_v, h_{lv}, σ and p_v compiled by NIST [20]. The contribution of W_{irr} in relation (2) is small and has been neglected. The ranges of the recoiling ^{12}C and ^{19}F atoms, R_C and R_F, are included in table 1 for comparison at the quoted values for the threshold energies $E_c(T)$.

It is interesting to note that at, for example, 20 °C, most of the work required to create a critical bubble is spent in evaporating the liquid, $W_{ev} = 80$ keV, the work required for creating the liquid–vapour interface amounts to $W_{lv} = 36$ keV and the mechanical work done during bubble expansion amounts to $W_m = -4.6$ keV. These contributions are affected by errors at the level of 15–20% due to uncertainties in the thermodynamic parameters (and these uncertainties increase with temperature).

The specific energy losses in liquid C_4F_{10} of the particles used in the calibration measurements discussed below, i.e α-particles and neutron-induced fluorine and carbon recoil nuclei, were calculated with SRIM [21]; the results are shown in figure 1. For the energy range considered here, with $5\,\text{keV} < E_{F,C,\alpha} < 500\,\text{keV}$, fluorine always has the higher stopping power, followed by carbon and α-particles. The stopping power at the Bragg peak of α-particles almost equals the stopping power of fluorine below 100 keV.

3. Detectors and read-out

The current PICASSO detector generation consists of cylindrical modules of 14 cm diameter and 40 cm height [5]. They are fabricated from acrylic and are closed on top by stainless steel lids sealed with polyurethane O-rings. Each detector is filled with 4.5 litres of polymerized emulsion loaded with droplets of C_4F_{10}; the droplet volume distribution peaks at diameters of around 200 μm. The active mass of each detector is typically around 85 g. The active part

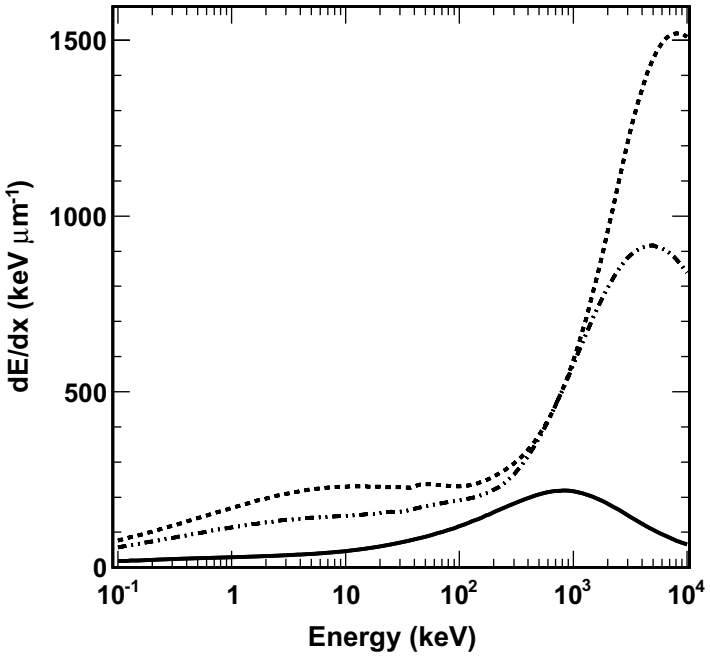

Figure 1. Stopping power in keV μm^{-1} for α-particles (continuous), fluorine nuclei (dotted) and carbon nuclei (dash-dotted) in C_4F_{10} calculated with SRIM [21]. In the energy range below 500 keV fluorine always has the higher dE/dx.

of each detector is topped by mineral oil, which is connected to a hydraulic manifold. After a measuring cycle, the detectors are compressed at a pressure of 6 bar to reduce the bubbles into droplets and to prevent bubble growth, which could damage the polymer. The operating temperature of the modules is controlled with a precision of $\pm 0.1\,^{\circ}$C. Each detector is read out by nine piezoelectric transducers. Three transducers are distributed around the detector at each of three different heights. They are flush mounted on a flat spot milled into the acrylic. The transducers are ceramic discs (PZ27 Ferroperm) with a diameter of 16 and 8.7 mm thickness and a sensitivity of 27 μVμbar^{-1}. The piezoelectric sensors are read out by custom made low-noise preamplifiers that serve a double purpose: providing impedance conversion and strong amplification (gain $\times$ 3000 between 0.5 and 130 kHz). The bandwidth of the amplified signal is limited to the range of 1–80 kHz using a series of customizable RC filters. The amplified output signal is digitized using a 12-bit analogue to digital converter (ADC) with serial output. The maximum amplitude of the digital signal is ± 2 V.

The trigger threshold is individually set for each channel, normally at ± 300 mV. The trigger condition requires at least one signal from a detector module crossing the threshold and, in this case, will initialize the read-out of all channels from this module. The system stores 8192 samples at a sampling frequency of 400 kHz, with 1024 samples before the trigger time. The total recorded signal is 20.48 ms long.

4. Energy calibration with the α-emitters ^{241}Am and ^{226}Ra

Two detectors were prepared especially to study the response of superheated liquids to α-decays of known origin. In one detector, the polymer in which the droplets are suspended was first

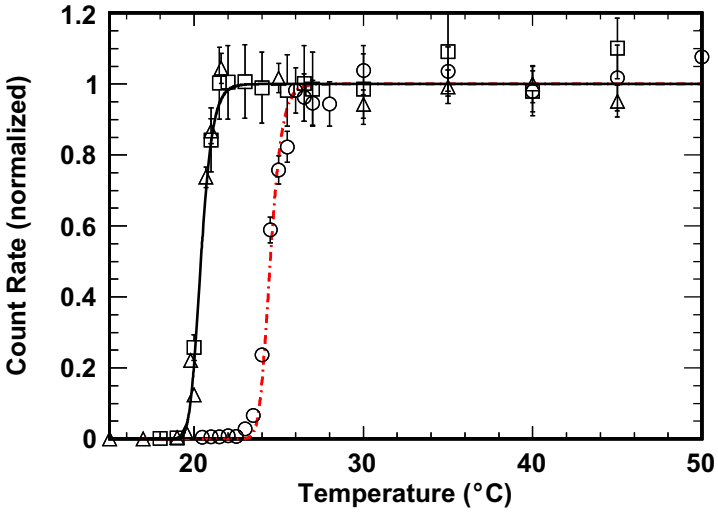

Figure 2. Response of detectors spiked with the α-emitters ^{241}Am and ^{226}Ra. The curve with the higher threshold temperature was obtained after spiking the detector matrix (but not the droplets) with ^{241}Am (circles) so that only α-particles entering the droplets can induce nucleation. At threshold only α-particles with energy depositions at the Bragg peak trigger nucleation. The lower threshold was obtained with two ^{226}Ra-spiked detectors (squares and triangles). Here the recoiling ^{210}Pb nucleus with the highest recoil energy in the decay chain ($E_{\mathrm{rec}} = 146\,\mathrm{keV}$) defines the threshold. The rates $\mathrm{g}^{-1}\mathrm{h}^{-1}$ following the Am and Ra spikes differ by a factor of 80; shown here are the respective count rates of the three measurements normalized at their plateau values.

spiked with an aqueous solution of ^{241}AmCl with an activity of 6.4 Bq, and after completion of the measurements, the same detector was spiked with 10 Bq of ^{226}Ra by injecting locally with a syringe an aqueous solution of RaCl. The other detector was exclusively spiked with 10 Bq of ^{226}Ra. Both detectors were shortened versions, 1/3 in height of normal PICASSO modules. The active mass of liquid C_4F_{10} amounted to 17.8 ± 2 g in the first and 26 ± 3 g in the second detector, which corresponds to volume loading fractions of $0.84 \pm 0.08\%$ and $1.2 \pm 0.1\%$, respectively. Both detectors were read out in one horizontal transducer plane, i.e. by three piezoelectric sensors arranged under 120° with respect to each other and mounted on the outside of the detector wall. The observed count rates as a function of temperature are shown in figure 2.

^{241}Am decays follow the reaction $^{241}\mathrm{Am} \rightarrow {}^{237}\mathrm{Np} + \alpha + 5.64\,\mathrm{MeV}$. The count rate of the ^{241}Am-spiked detector exhibits a threshold at 22 °C, reaches a flat plateau at 26 °C and traverses 50% of the plateau rate at 24.5 °C. This temperature corresponds to an energy threshold of $E_{\mathrm{th}}(24.5°) = 71\,\mathrm{keV}$ according to neutron calibrations (section 5). The measured count rate at the plateau corresponds to 0.34 ± 0.02 cts $\mathrm{g}^{-1}\,\mathrm{h}^{-1}\,\mathrm{Bq}^{-1}$, which is close to the expected count rate of 0.47 ± 0.11 cts $\mathrm{g}^{-1}\,\mathrm{h}^{-1}\,\mathrm{Bq}^{-1}$, assuming a uniform distribution of α emitters outside the droplets. This estimate is based on the geometric efficiency that an α-track hits a droplet, which is given by the relation

$$\epsilon_\alpha = \frac{4}{3} f \frac{R_\alpha}{R_{\mathrm{d}}}, \tag{4}$$

where f is the loading of the detector ($0.84 \pm 0.08\%$), R_α is the range of the α-track ($37\,\mu$m) and R_d is the average droplet radius ($200 \pm 50\,\mu$m), yielding $\epsilon_\alpha = 0.21 \pm 0.05\%$.

As described later in section 9.2, similar distributions of acoustic energy released from AcBe neutrons and these ^{241}Am αs confirm that the ^{241}Am α-emitters are predominantly located outside the droplets. Therefore, the only α-particles that trigger a phase transition at the 22 °C threshold are those with the highest specific energy deposition, which corresponds to the Bragg peak. At higher temperatures the liquid becomes sensitive to smaller $\mathrm{d}E/\mathrm{d}x$ on the tracks, but since most of the αs are stopping inside the droplets and are thus able to trigger at the threshold with their Bragg peak, the temperature response levels off to a plateau. The contribution of tracks where the Bragg peak is in the matrix and the α-particle continues into the droplet with lower $\mathrm{d}E/\mathrm{d}x$ is expected to create an ascending slope of less than 5% above 30°, which is smaller than the uncertainties of the measurements.

After completion of data taking with the ^{241}Am spike, the same detector was loaded with ^{226}Ra ($T_{1/2} = 1602$ years). ^{226}Ra decays into ^{222}Rn ($T_{1/2} = 3.8$ d), which then decays following the sequence of transitions $^{222}\mathrm{Rn} \rightarrow {}^{218}\mathrm{Po} \rightarrow {}^{214}\mathrm{Pb} \rightarrow {}^{214}\mathrm{Bi} \rightarrow {}^{214}\mathrm{Po} \rightarrow {}^{210}$ Pb via three α- and two β-decays; the rest of the chain is too long-lived to be relevant here. The energies of the emitted α-particles are 5.49, 6.0 and 7.69 MeV, respectively, and the half-lives are short with respect to the ^{226}Ra half-life (3.8 d, 3 min, 27 min, 19 min, 0.2 ms). By visual inspection of the positions of the bubbles formed, the α-activity could be observed to diffuse slowly within several days from the point of injection over the entire detector volume. After 14 d the count rate in the detector had reached asymptotically its maximum value and data were taken as a function of temperature. The results are shown in figure 2.

The observed threshold is now shifted by about 4 °C towards lower temperatures, indicating that the energy depositions are larger: the threshold starts at 19 °C and reaches its plateau at 22 °C. However, the observed shift cannot be attributed to the energy deposition of the α-particles emitted by the Ra-chain, since they have the same maximum stopping power at the Bragg peak than those emitted in ^{241}Am-decay; rather the reduced energy threshold is now caused by ^{210}Pb nuclei recoiling inside the droplets with an energy of 146 keV, since this is the nucleus with the highest recoil energy in the chain.

By further raising the temperature, the detector becomes subsequently sensitive to the lower energetic ^{214}Pb (112 keV) and ^{218}Po (101 keV) recoil nuclei. First ^{214}Pb recoils add to the observed count rate, but once the energy threshold is low enough to allow ^{218}Po recoils to trigger, the ^{214}Pb recoils, which follow ^{218}Po decays ($T_{1/2} \approx 3$ min), are no more able to contribute several minutes after run start. This is due to the fact that once a phase transition has occurred in a droplet it is no longer sensitive to subsequent energy depositions. The same situation arises for ^{214}Po-decays, which are gradually rendered undetectable following $^{222}\mathrm{Rn}/^{218}$Po-decays in the same droplet for measuring times exceeding the half-lives of the two β-decays after run start ($T_{1/2} = 27$ and 19 min). This expected asymptotic decrease in count rate due to the depletion of ^{214}Po-decays has been observed for temperatures $T > 20$ °C and for measuring times lasting up to 2 h after run start. In order to eliminate this time dependence, the count rates shown in figure 2 were always calculated for the same time interval after run start.

The observed threshold curve is characterized by a steep slope, but the data are not precise enough to reveal a step-like substructure that should be caused by the 34 keV energy difference between the ^{214}Pb and ^{210}Pb recoils. However, the 146 keV recoil energy of the ^{210}Pb nuclei at the observed threshold temperature is consistent with the threshold obtained for neutron-induced ^{19}F recoils discussed in section 5. By increasing the temperature from 22 to 25 °C,

the ^{226}Ra-spiked detector also becomes sensitive to α-particles, but since the detector is already fully sensitive, the count rate remains unaffected. However, above 25 °C, α-particles contribute to the amplitude of the acoustic signal. This effect will be described in section 9.

Since the ^{241}Am activity is still present after the ^{226}Ra spike and since the threshold temperature for detection of the ^{241}Am α-particles is about 4 °C higher than the threshold of the ^{226}Ra spike, one would expect to observe a step at 22 °C in figure 2. The absence of this feature can be explained by the fact that after adding the Ra-spike the absolute count rate increased by a factor of 80 and the specific rate by a factor of 47 to 16 ± 1.1 cts g^{-1} h^{-1} Bq^{-1}.[17] This strong increase in count rate is not yet completely understood. Assuming a uniform distribution of α-emitters in the matrix and the droplets, the count rate should be determined essentially by the loading fraction and would result in an expected rate of 1.7 ± 0.2 cts g^{-1} h^{-1} Bq^{-1}, only 12% of the observed count rate. A possible explanation would be a substantial ($\times 8.4$) increase in concentration of α-emitters in the droplets, possibly caused by an increased solubility of ^{222}Rn in fluorocarbons such as C_4F_{10} compared with the ^{222}Rn solubility in the water-based polymer.

The second detector used in this study, similar in size and composition but spiked exclusively with 10 Bq ^{226}Ra, reproduced the above-described threshold results (figure 2). Also, its count rate, normalized to the active mass of C_4F_{10}, was found to be comparable to that of the Am-loaded detector after the Ra spike with 13 ± 3 cts g^{-1} h^{-1} Bq^{-1} [22].

Another similar study of α-emitters has been described by Hahn [23] employing ^{238}U and ^{232}Th spikes in CCl_2F–$CClF_2$ operated under negative pressure. In those measurements, recoils from ^{210}Po α-decays could be clearly separated from the 67 keV smaller recoil energies produced in ^{212}Po-decays.

5. Energy calibration with mono-energetic neutrons

The dependence of the threshold energy E_{th} on temperature and pressure was studied with neutron-induced nuclear recoils. For this purpose, extensive calibrations were performed at the Montreal Tandem van de Graaff facility with mono-energetic neutrons ranging from $E_{\mathrm{n}} = 4.8$ keV to 4 MeV. In the case of nuclear recoils induced by neutrons of low energy, the interaction is mainly through elastic scattering on fluorine and carbon nuclei. Inelastic collisions occur only if the centre-of-mass kinetic energies of the neutrons are higher than the first excitation level of the nuclei (1.5 and 4.3 MeV for ^{19}F and ^{12}C, respectively). Absorption of neutrons by the ^{19}F nucleus followed by α-particle emission requires a neutron energy of 2.05 MeV.

Assuming neutron elastic scattering on nuclei, the recoil energy, E_{R}^{i}, of the nucleus i is given by

$$E_{\mathrm{R}}^{i} = \frac{2 m_{\mathrm{n}} m_{N_i} E_{\mathrm{n}} (1 - \cos\theta)}{(m_{\mathrm{n}} + m_{N_i})^2}, \tag{5}$$

where E_{n} and θ are the incident neutron energy and the neutron scattering angle in the centre-of-mass system, and m_{n} and m_{N_i} are the masses of the neutron and the nucleus N_i, respectively. At a given neutron energy E_{n}, the recoiling nuclei are emitted with an angular distribution, every angle being associated with a specific recoil energy ranging from 0 keV at $\theta = 0$ to the maximum energy $E_{R,\max}^{i}$ for $\theta = 180°$. At the small energies considered here, the angular

[17] This does not appear in figure 2 since all rates are normalized to a common plateau value.

Table 2. Five of the resonances of the ^{51}V(p, n)^{51}Cr reaction used for neutron calibration. All five resonances have sub-keV intrinsic widths [24].

Resonance	E_p (MeV)	E_n (keV)
I	1.568	4.8
V	1.598	40
VII	1.607	50
VIII	1.617	61
XI	1.651	97

distribution is isotropic in the centre-of mass system and the recoil energy spectrum dR^i/dE^i_R has a rectangular, box-like shape up to $E^i_{R,\max}$:

$$E^i_{R,\max} = f_i E_n = \frac{4 m_n m_{N_i} E_n}{(m_n + m_{N_i})^2}. \tag{6}$$

The factor f_i gives the maximum fraction of the energy of the incident neutron transmitted to the nucleus i, where $f_F = 0.19$ and $f_C = 0.28$ for ^{19}F and ^{12}C, respectively.

The mono-energetic neutrons used for calibration were produced via nuclear reactions with mono-energetic protons via the ^{7}Li(p, n)^{7}Be and ^{51}V(p, n)^{51}Cr reactions. The measurements with the Li target ($10\,\mu g\,cm^{-2}$) cover a range of neutron energies from 100 keV to 4 MeV and the results obtained are discussed in detail in [18]. With improved proton beam stability these calibrations were recently extended in PICASSO with a ^{51}V target ($9\,\mu g\,cm^{-2}$) down to 4.8 keV. To acquire sufficient statistics close to threshold, the proton beam energies were tuned to individual resonances in the ^{51}V(p, n)^{51}Cr reaction cross section [24]. In particular the five resonances quoted in table 2 have been selected, each of which has an intrinsic width below keV.

The detectors used for these measurements are smaller in size (63 ml) with an active mass of 1 g of C_4F_{10}, but were fabricated in the same way and with similar droplet dimensions as the standard 4.5 litre detectors. For each of the selected neutron energies, data were taken at $\theta \approx 0^\circ$ with respect to the beam while ramping the temperature up and down for a given pressure. Since close to threshold the cosmic ray-induced n-background can amount to 50% of the total count rate, each neutron run at a fixed temperature was followed by a background run at the same temperature (after 8 h of recompression).

For a fixed neutron energy the data have been normalized by the integrated proton current and the count rate of a ^{3}He counter mounted behind the target was used to compensate for short off-resonance beam energy fluctuations [25]. The measurements at the lowest neutron energy (4.8 keV) were particularly challenging, since at the threshold and above, the detectors had to be operated between 48 and 60 °C where C_4F_{10} becomes sensitive to the 320 keV γ-rays ($T_{1/2} = 28$ d) following de-excitation of ^{51}Cr. Therefore this background had to be measured independently during a beam off period after each neutron run and subtracted from the data.

The recorded count rates for the Li and V targets at different neutron energies at ambient pressure and as a function of temperature are compiled in figure 3. From these measurements, the threshold temperature, T_{th}, can be extracted for a given neutron energy by fitting the data to a theoretical response function including energy losses in the target and the detector matrix and by keeping the intrinsic energy resolution as a free parameter (section 7). Here the threshold temperature is defined as the temperature at which 0.5% of the nuclear recoils will cause a

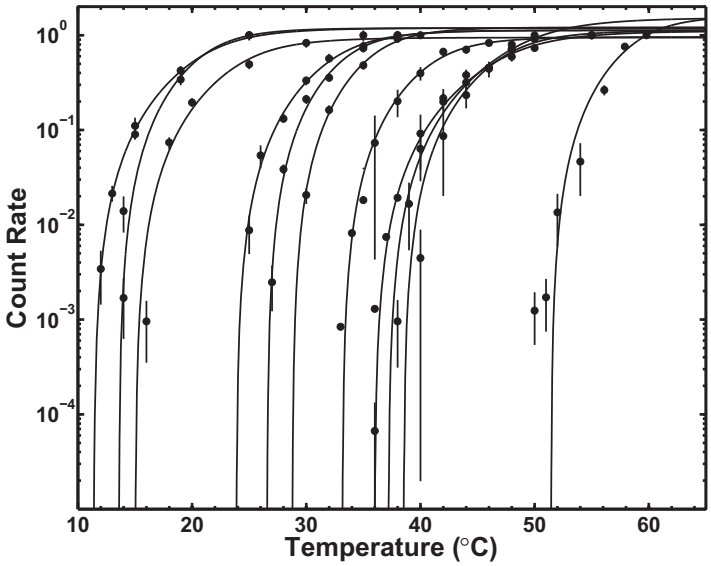

Figure 3. Detector response to mono-energetic neutrons as a function of temperature (°C). The detectors were 10 and 15 ml modules loaded with C_4F_{10} droplets. From left to right the threshold curves correspond to neutron energies of 4 MeV, 3 MeV, 2 MeV, 400 keV, 300 keV, 200 keV, 97 keV, 61 keV, 50 keV, 40 keV and 4.8 keV, respectively. The five lowest energies were obtained from resonances of the $^{51}V(p, n)^{51}Cr$ reaction, the higher energy neutrons were produced with the $^{7}Li(p, n)^{7}Be$ reaction; several more energies obtained with the Li target are shown in figure 4. The curves shown are fits, which include attenuation and resolution effects from simulations.

phase transition. From this the neutron threshold, energy as a function of temperature can be inferred as is shown in figure 4. For the energies considered here, $E^{n}_{th}(T)$ follows an exponential dependence on temperature. A similar exponential trend was observed by other authors for a series of halocarbons such as C_4F_8, CCl_2F_2, $C_2H_3ClF_2$ and $C_2Cl_2F_4$ [13].

For WIMP searches it is important to know the minimum nuclear recoil energy that produces a bubble as a function of temperature. Due to the composition of the target in use, C_4F_{10}, there are two possibilities in converting neutron energy into recoil energy: (i) if the response depends on the energy that is deposited on the entire recoil track, then the threshold should be attributed to the more energetic carbon nucleus; (ii) if the recoil nucleus with the greater dE/dx triggers, then it is fluorine that defines the threshold. In both the cases, the energy thresholds (at 1 bar) are obtained from an empirical fit to the neutron threshold data and in the case of ^{19}F follow the relation

$$E^{F}_{th}(T) = f_F E^{n}_{th} = (4.93 \pm 0.15) \times 10^3 \exp(-0.173\, T(^{\circ}C))(\text{keV}). \quad (7)$$

The error of 3% is largely due to the systematic errors of $\pm 0.2\,^{\circ}C$ in the temperature measurement during the test beam runs. Given the temperature range of operation in PICASSO, this translates in the case of ^{19}F recoils into a range of sensitivity from $E_F > 2.0$ keV at 45 °C to $E_F > 200$ keV at 18.5 °C, respectively.

Several observations support the conclusion that indeed fluorine atoms with their higher dE/dx are responsible for defining the threshold: (i) the neutron scattering rate on ^{19}F is four

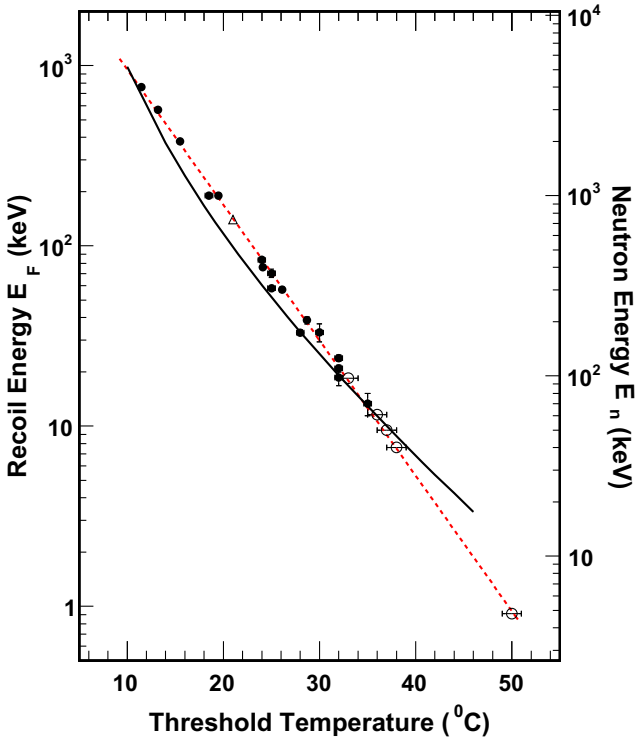

Figure 4. Relationship between the energies of mono-energetic neutrons (right vertical scale) and the temperature measured at the threshold (figure 3); the left vertical scale displays the maximum recoil energy of fluorine, which corresponds to the selected neutron energy. For fluorine recoil energies from $E_F = 0.9$ to 760 keV, the data are well described by an exponential dependence on temperature (broken line). The open triangle at 21 °C corresponds to the energy deposition of 146 keV of ^{210}Pb recoils following ^{222}Rn-decay (figure 2). The continuous line represents $E_c(T)$ calculated in relation (2); it is the work required for creating a bubble with a critical radius $R_c(T)$.

to six times larger than the cross section on ^{12}C in the considered energy range with substantial enhancement in its resonances. If carbon would trigger first, a second threshold should be observed in the threshold curves of figure 3 at higher temperatures when scattering on ^{19}F sets in. Measurements carried out at on- and off-resonance energies in the ^{19}F cross section indicate that fluorine determines the threshold; (ii) the detection threshold for the 146 keV recoil ^{210}Pb nuclei following α-decays of ^{214}Po matches the one for ^{19}F at the same energy; (iii) for recoil energies between 10 keV and 1 MeV, the critical energy $E_c(T)$ for bubble formation predicted by the Seitz model follows closely the ^{19}F threshold; (iv) measurements with C_4F_8 and $C_2Cl_2F_4$ show that the recoil energy of the species with the higher dE/dx matches well the predicted $E_c(T)$ [13, 16].

At temperatures below 40 °C, an up to 30% departure of the measured thresholds from the calculated $E_c(T)$ values is recorded, and for threshold energies smaller than 10 keV, data and theory start to deviate significantly from each other. The causes of these discrepancies are not yet well understood. The dominant contributions for the work required to create a critical bubble

at the temperatures involved are due to evaporation and interface formation. It was observed for halocarbons that E_c approaches zero if the temperature attains 90% of the critical energy T_c, which would correspond to 74 °C in the case of C_4F_{10} [18]. This temperature is also very close to the limit of stability observed during studies of γ-sensitivity of superheated liquids, as discussed in section 6. By tentatively forcing the surface tension to rejoin zero at $0.9T_c$ a better fit to the data can be obtained, but still with an offset of −30% for temperatures between 20 and 40 °C. The observed disagreement is suspected to be due to a still incomplete description of the underlying processes, once the critical radius R_c approaches the nanometer scale.

Also at the low-temperature side the theoretical description of the Seitz model appears incomplete, since thermodynamics requires that the threshold curve bends up towards infinity at the boiling temperature $T_b = -1.7$ °C.

6. Energy response to γ-rays

In contrast to the energy depositions of recoiling nuclei and α-particles, the main interaction process of γ-rays with the detector material occurs via Compton scattering. Because of their very small stopping power, recoiling Compton electrons cannot trigger a phase transition directly in the normal temperature range of operation. Rather the observed sensitivity to γ-rays is attributed to δ-rays or Auger electrons scattered randomly along the tracks of the Compton electrons. These low-energy electrons curl up at the end of their trajectory into highly localized clusters of ionization or hot spots, which rarely lead to energy depositions at the keV level. In particular, it was found in simulations that the δ-ray energy spectra on tracks of electrons from 5 keV up to 500 keV and on tracks of 1 GeV muons are very similar in shape, and 50% of the emitted δ-rays were found to deposit energies smaller than 0.05 keV [18, 26]. Calibrations with γ-rays can therefore give only information about the probability distribution of clusters of energy on the tracks of Compton electrons.

Such a study was performed with a ^{22}Na source (0.7 μCi), which yields 1.275 MeV γ-rays, as well as the two 511 keV photons from e^+e^- annihilation. Compton scattering of the 1.275 MeV γ-rays produces recoiling electrons in the detector medium with an average energy of 500 keV and with a range of 1.1 mm, whereas the annihilation photons create electrons of 170 keV. Two different detectors were used: a standard 4.5 l detector with an active mass of 78.9 ± 8 g to explore the low-temperature response from 40 to 50 °C and a 10 ml detector with an active mass of 30 mg to measure temperatures from 48 up to 72 °C [26, 27]. The count rates as a function of temperature are shown in figure 5 and it was found that the measured sensitivity can be fitted over more than 10 orders of magnitude with a sigmoid function

$$\epsilon_\gamma = \frac{\epsilon_0}{1 + \exp(T_0 - T/\tau)}, \tag{8}$$

with $T_0 = 63.6$ °C and $\tau = 1.78$ °C. At the plateau, the measured efficiency ($\sim 5\%$) corresponds roughly to the geometric efficiency that a Compton electron hits a droplet ($\sim 1\%$); the observed difference can be explained partly by the uncertainties in the droplet size distribution and the active mass of the 10 ml detector used. Measurements with other sources (^{57}Co, ^{60}Co, ^{137}Cs) showed that the response curves are identical and that the plateau efficiencies are comparable for γ-energies from 127 keV to 1.3 MeV. This is expected, since for an average Z of the detector material of $Z \approx 5.5$, the Compton scattering cross section dominates in the energy range from 400 keV to 5 MeV and the mass attenuation coefficient does not vary much.

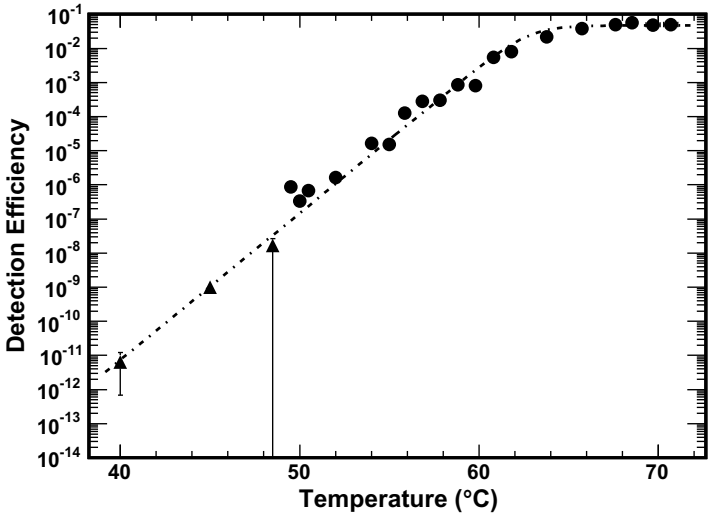

Figure 5. γ-ray sensitivity as a function of temperature (°C). The data at the four lower-temperature points were recorded with a standard 4.5 litre detector (triangles); the higher-temperature data were taken with a small 10 ml detector. At the plateau the γ-detection efficiency is determined by the geometry and probability that a Compton electron hits a droplet. Over 10 orders of magnitude in count rate the data are well reproduced by the sigmoid function described by relation (8). After 72° the detector becomes sensitive to spontaneous nucleation.

In addition, the stopping power of the scattered electrons does not vary much in this region and since the δ-ray production probability is proportional to the $\mathrm{d}E/\mathrm{d}x$ on the particle track, the γ-detection efficiency reflects the constant production efficiency of δ-electrons. This scenario was confirmed by simulations, which in addition show that the sigmoid shape of the observed response curve can be reproduced well [18, 26].

Above 72 °C the detector becomes sensitive to spontaneous nucleation. An increase in temperature by 1° leads to an increase in count rate by approximately 3 orders of magnitude.

7. Energy resolution

On inspection of the α data in figure 2, it is apparent that the detection threshold is a well-defined but not sharp step function; the count rate increases steeply but gradually from the threshold to full efficiency. The probability $P(E_{\mathrm{dep}}, E_{\mathrm{th}})$ that an energy deposition E_{dep} larger than the energy threshold E_{th} will generate a nucleation can be approximated by

$$R(E_{\mathrm{dep}}, E_{\mathrm{th}}(T)) = 1 - \exp\left[a\left(1 - \frac{E_{\mathrm{dep}}}{E_{\mathrm{th}}(T)}\right)\right], \tag{9}$$

where the parameter a describes the observed steepness of the threshold: the larger the a is, the sharper the threshold is defined. This parameter is related to the intrinsic energy resolution and reflects the statistical nature of the energy deposition and its conversion into heat [28]. It has to be determined experimentally for each superheated liquid and for different particle species, respectively. Our measurements with α-emitters with well-defined, mono-energetic recoil nuclei (^{210}Pb) indicate a threshold that can be described best with $a = 10 \pm 1$ at 146 keV; α-particles

depositing their energy at the Bragg peak seem to produce a somewhat less steep threshold described by $a = 5.8 \pm 0.7$ at 71 keV (figure 2).

This parameter is more difficult to extract from calibrations with mono-energetic and poly-energetic neutrons due to the continuous spectral distributions of the recoiling nuclei. Our data with mono-energetic neutrons above 400 keV are compatible with $a = 10 \pm 5$; at lower energies, smaller values appear favoured with $a = 2.5 \pm 0.5$ [29]. A more precise study of a suspected temperature dependence of the resolution parameter is the subject of ongoing measurements.

8. Determination of the critical length L_c

The relatively good agreement between deposited energy at threshold E_{dep} and the critical energy E_c required for nucleation below 40 °C observed in neutron calibrations allows an estimate of the effective ion track length $L_c = bR_c$ over which the energy deposition is distributed. We follow here the model proposed by d'Errico, which assumes that the vapour cavity formed initially may extend along the charged particle track, before ending up in at least one structure of spherical shape of size R_c [13].

8.1. L_c from α-emitters

In the case of α-particles, the threshold energy E_{th}(T) for particles entering from outside the droplets is related to the deposited energy by relation (3) where $(dE/dx)_{Bragg} = 210\,\text{keV}\,\mu\text{m}^{-1}$ is the maximum specific energy loss at the end of the track of a 5.64 MeV α-particle emitted in ^{241}Am-decays. Using (3) and $E_{th}(T) = 71$ keV, it follows that $L_c = 0.33\,\mu$m, for the critical length L_c along which the particle deposits its energy in order to be able to create a critical proto-bubble. Using in addition the prediction by the Seitz model given in (1) for the critical radius $R_c(T)$, one obtains $L_c(24°) = 3.8 \times R_c(24°)$, which yields an estimate of the model parameter $b_\alpha(24°) = 3.8$ for this temperature. This value is compared in figure 6 with those obtained from neutron calibrations.

On the other hand, one can use the fact that α-particles do not trigger phase transitions at 21 °C and $E_{dep} = 146$ keV in order to obtain an upper limit on the critical length of $L_c(21°\text{C}) \leqslant 0.45\,\mu$m, which implies $b_\alpha(21°\text{C}) \leqslant 5$, as indicated in figure 6.

Incidentally, these values of L_c are close to the range of ^{19}F at this threshold energy, but definitely smaller than the range of ^{12}C with $R_C = 1.16\,\mu$m. Since from figure 1 the stopping power of carbon is always smaller than that of fluorine, its energy deposition would be around 80 keV and therefore smaller than the 146 keV required, which supports the assumption made in section 5 that fluorine triggers at the threshold.

8.2. L_c from neutron-induced recoils

Using (3) and the threshold energies E_{th}(T) obtained for nuclear recoils in the neutron calibrations described in section 5, two sets of parameters b_F(T) and b_C(T) result, depending on the assumption of whether either ^{19}F recoils trigger at threshold or ^{12}C recoils (lower and upper curves, respectively in figure 6). Both curves represent lower bounds on L_c. In particular, in the case of b_F the area between the two curves is allowed, since above that region carbon would trigger at the threshold [28]. The two estimates for L_c discussed in the α scenario add two independent constraints which favour the lower set of b_F values. The range of the preferred

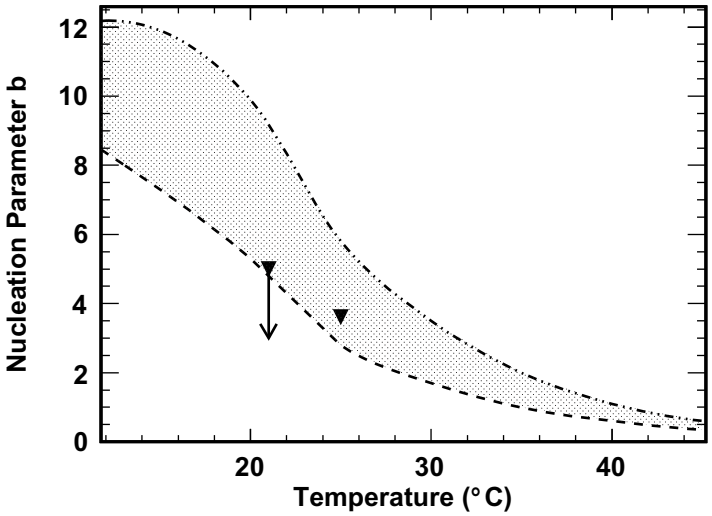

Figure 6. The nucleation parameter b as a function of temperature. This parameter uses $L_c = bR_c$ to relate the spatial extension of the energy deposition with the critical radius defined in relation (1). If carbon would trigger at the threshold, then only nucleation parameters above the upper line would be allowed. If fluorine recoils determine the threshold, then the shaded region between the two curves defines the allowed parameter space. The threshold data of the α-spiked detectors yield an additional upper limit at 21 °C and an additional prediction at 25 °C (triangles); the α data favour the lower part of the shaded parameter space.

values, together with the observed trend that b increases with temperature, agrees well with measurements on several other halocarbons discussed in [13].

9. Acoustic signals from particle-induced events in superheated liquids

It is known that energetic charged particles traversing non-stressed liquids or solids produce acoustic waves during their passage. This so-called thermo-acoustic effect was predicted and described by Askaryan *et al* [30] and is exploited in high-energy neutrino detection in the PeV range by the ANTARES and ICECUBE experiments [31, 32]. However, applied to the processes considered here, with energy depositions in the keV range, the emitted sound intensities predicted by the thermo-acoustic effect are undetectable. On the other hand, particle interactions in stressed or superheated liquids produce detectable acoustic signals that are related to the nature or the extension of the primary event; this suggests that the phase transition process in superheated liquids provides an intrinsic acoustic amplification mechanism with a gain of at least 10^5 [33].

9.1. Neutron-induced recoils

Calibration data with fast neutrons of AcBe, AmBe and Cf sources showed that the associated waveforms have a short rise time, reaching the maximum amplitude after 20–40 μs, with slower oscillations following for several milliseconds. To characterize signals of different origins in

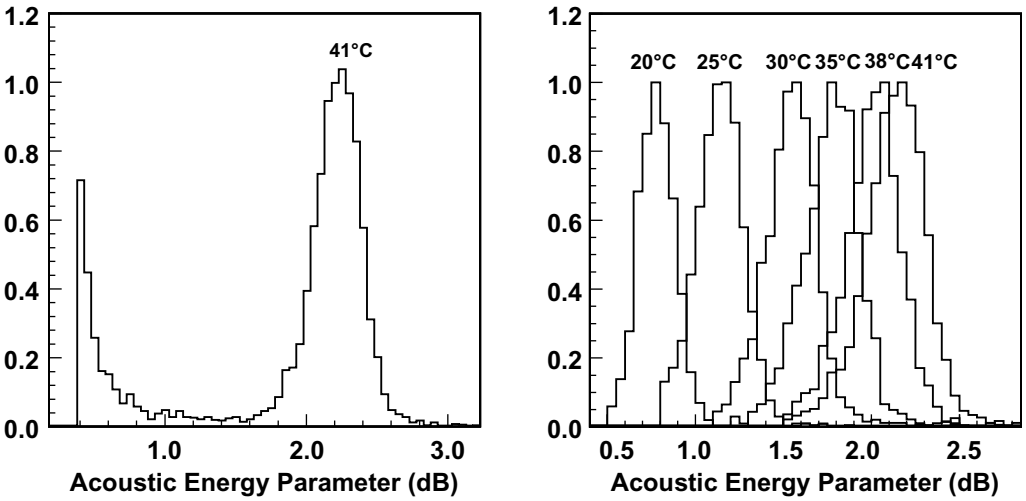

Figure 7. Distribution of the acoustic energy parameter recorded in calibrations with poly-energetic neutrons from an AmBe source. For a given event the signal energy is constructed by squaring the amplitudes and averaging over the waveforms of at least six transducers per detector. The logarithm of this quantity is used to define the acoustic energy parameter. Neutron-induced recoils show up in a peak (the same peak where WIMP-induced recoils are expected); this peak is well separated from acoustic and electronic noise (left) and shifts with increasing temperature to larger signal intensities (right).

the detector, a Bessel band-pass filter is applied to cut off frequencies below 18 kHz and then the waveform of each transducer is squared and integrated over the signal duration, starting from a fixed pre-trigger time. The resulting values are then averaged over all active transducers for each event in order to mitigate solid angle effects. The logarithm of this averaged acoustic energy is used to define the acoustic energy parameter, so called as it is a measure of the average energy contained in the transducer signals. The resolution at full-width at half-maximum of this distribution is around 20% for temperatures tested, while the centroid of this distribution increases smoothly with increasing temperature (figure 7). The noise peak at low values of the acoustic parameter is mostly due to electronic spikes and acoustic events occurring in neighbouring detectors; its width increases with temperature, but remains for all temperatures well separated from the signal peak[18].

This property can be used to discriminate particle-induced recoil events from non-particle-related signals [5, 34]. Since WIMP-induced recoils are similar to neutron-induced recoils, this feature is of prime importance for dark matter searches with superheated liquids.

9.2. α-decays

α-decays in the PICASSO detectors also produce signals with well-defined acoustic energy, and if fully contained in a droplet, with larger acoustic energy than observed in neutron-induced events [6]. This can be explained by the fact that the ranges of neutron-induced recoils of keV

[18] The values of the acoustic parameters in figures 7, 8, 10 and 11 differ from each other due to different experimental conditions such as amplifier gains and a steadily refining analysis; still in each graph the same definition is being used for both neutrons and α's (γ's) and for different temperatures.

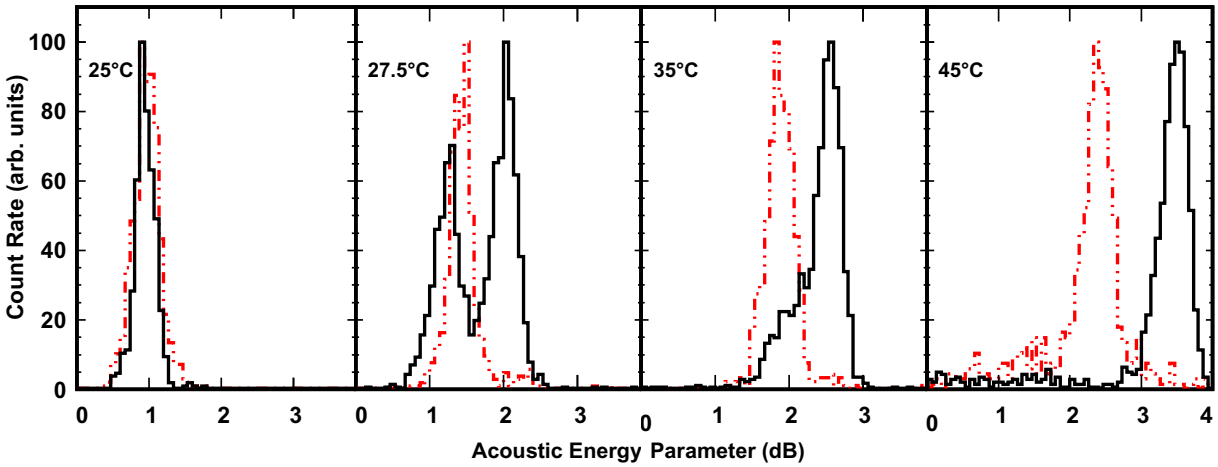

Figure 8. Distributions of the acoustic energy parameter observed as a function of temperature with α-contaminated detectors where the α-activity occurs inside the droplets. The dotted histograms indicate the location of recoil events produced during calibrations with an AcBe neutron source. Left (24 °C): the signal strengths of recoil nuclei in α-decays coincide with those from neutron calibrations. Centre (27.5 °C): a second peak appears on the high side, which is caused by the joint effect of recoil nuclei and the energy deposition by the α-track. There are still events where only recoils nucleate (neutron data were taken at 28 °C and are therefore slightly shifted to the right). Right (45 °C): at this temperature, α-particles and recoil nuclei contribute simultaneously to the signal.

energies are of sub-μm extension and therefore comparable in size to the critical length L_c. Therefore these events are able to trigger only one primary nucleation. However, α-emitters located within the superheated liquid can trigger at least two vapourizations: one from the recoiling nucleus and the second one or more on the α-particle track. In both the cases, the energy released during vapourization increases with increasing temperature, but stays well defined for a given temperature.

Data taken with the α-spiked detectors described in section 4 have been used to investigate this nucleation hypothesis further. To detect possible deviations from single bubble nucleations, most of the α-measurements at a given temperature were followed by an exposure to an AcBe neutron source.

For the ^{226}Ra-spiked detector and regular 4.5 litre PICASSO detectors with high intrinsic α-background rates, the following pattern arises when the distribution of the acoustic energy parameter is recorded as a function of temperature (figure 8): between the threshold at 21 °C and below 25 °C, only recoil nuclei create a peak, which coincides with the location of the neutron-induced recoils during exposure to an AcBe source. With further increasing of the temperature to above 25°, when the detector becomes sensitive to α-particles, a second peak arises at higher acoustic energy and the first peak gradually diminishes. This second peak corresponds to nucleations due to recoil nuclei plus nucleations caused on the α-track first by the Bragg peak and then, with increasing temperature, by subsequently lower $\mathrm{d}E/\mathrm{d}x$ on the tracks. During this redistribution between the peaks, the sum of the count rates remains constant; the relative contributions to the total count rates are shown in figure 9. The apparent shift of +2 °C between the threshold data shown in figure 2 and the data shown in figures 8 and 9 is due to an

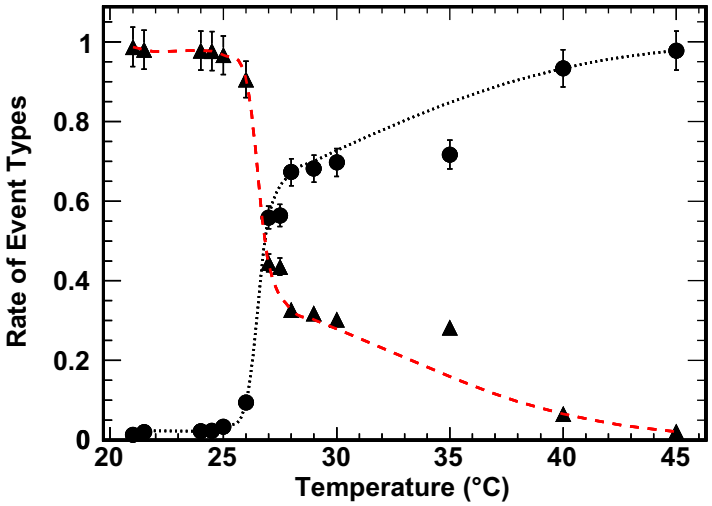

Figure 9. The two event types that contribute to the acoustic signal energy for α contaminations within the droplets: nuclear recoil-induced events corresponding to the first peak in figure 8 (triangles); joint contribution of nuclear recoils *and* α-particle-induced events corresponding to the second peak in figure 8 (dots). The first peak coincides with the acoustic energy parameter of neutron-induced recoils and dominates between 21 and 25 °C; above that temperature the detector becomes sensitive also to α-particles, which adds to the strength of the signal, but does not change the count rate, since the detector is already fully sensitive. Both contributions are constrained to sum to one and curves are drawn to guide the eye.

equivalent 0.2 bar difference in operating pressure: the spiked detectors (figure 2) were operated at 1 bar surface ambient pressure, whereas the data shown in figures 8 and 10 were taken at the SNOLAB underground site at 1.2 bar ambient pressure.

It was also noted that the degree of separation between recoils and α-particles depends on the temperature and the frequency content of the signals: at temperatures around 25 °C high-pass filters that accept frequencies above 10 kHz give the best result and the resolution tends to decrease with increasing cut-off frequency. The opposite happens at high temperatures—above 40 °C—where the best results are obtained with cut-offs above 100 kHz and discrimination worsens for lower cut-offs. These observations suggest that the fast component of the signal does not depend on the droplet size, but conveys information of the very first stage of bubble formation [8]. A plausible explanation of this effect will be given in section 10.

For the ^{241}Am-spiked detector described in section 4, where only α-particles originating from outside the droplets are able to trigger a phase transition, the signal energy distribution coincides with the distribution recorded during the neutron sessions over the considered temperature range, with a tendency towards larger acoustic energies, indicating an average probability slightly larger than one nucleation (figure 10). In contrast to the 27 °C data shown in figure 8, where the α-emitters were concentrated inside the droplets, the second peak is now absent.

From these observations with Am and Ra spikes, it can be expected that the limitation on the discrimination power will eventually come from the fraction of α-particles which only produce one bubble, just like nuclear recoils do. In this respect α-emitters located in the detector

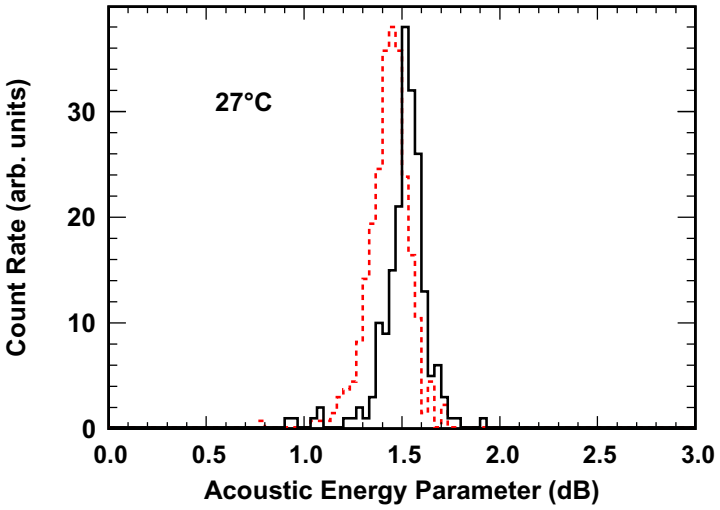

Figure 10. Distribution of the acoustic energy parameter observed at 27 °C with a detector spiked with the α-emitter ^{241}Am compared with the signals induced by fast neutrons from an AcBe source (dotted). Here the α-activity is located outside of the droplets. The α-peak is slightly displaced towards higher acoustic energy, but in contrast to the 27 °C data in figure 8, a second peak is absent.

matrix are of more serious concern in terms of unreducible background than contaminations within the droplets, provided the latter are large enough in diameter to contain most of the α-tracks.

9.3. δ-electrons from γ-ray-induced events

If detectors are operated at temperatures far below the plateau-γ sensitivity (i.e. 65 °C), then the clustered energy depositions from Auger- or δ-electrons on the tracks of Compton scattered electrons create events with small multiplicity within a droplet (section 6). Therefore, the acoustic signals are expected to reproduce those produced by single nucleations on the short tracks of nuclear recoils. In order to verify this hypothesis, data were taken with two different detectors in the presence of a ^{22}Na and a ^{137}Cs source, respectively, and compared with the signals induced by fast neutrons from a γ-shielded AcBe source. Measurements were carried out at 45, 46 and 50 °C, respectively, and the acoustic energies of the γ-induced signals coincided with those of the neutron-induced recoils (figure 11). It would be interesting in future to extend these measurements to higher temperatures, where also multiple nucleations might become observable on the Compton electron tracks traversing the droplets (the high temperature data in section 6 were taken without neutron reference measurements).

10. Dynamics of bubble growth and acoustic signal formation

The dynamics of bubble growth and the associated sound emission in superheated liquids is a complex phenomenon involving nonlinear thermodynamic processes, which are still the subject of ongoing research [35]. Particle-induced sound generation in superheated liquids was first discussed in [33], but until now only an approximative and qualitative description can

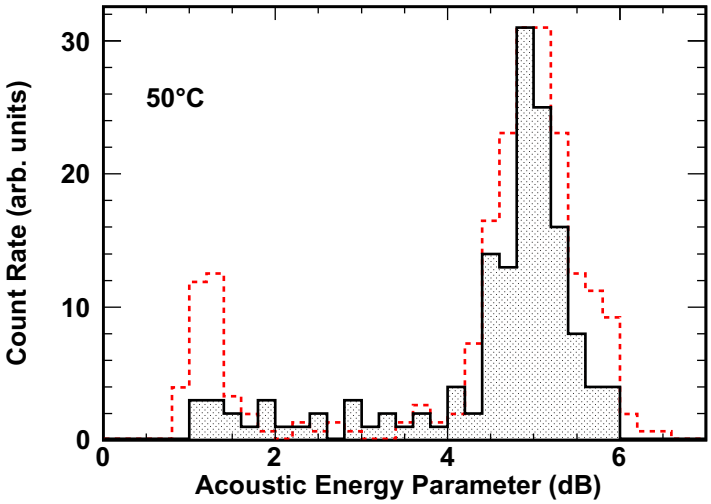

Figure 11. Acoustic energy parameter for γ-induced events. The data were taken in the presence of a ^{137}Cs source (shaded) and compared with the signals from a γ-shielded AcBe neutron source (dotted line). γ-induced events are caused by clustered energy depositions (Auger- or δ-electrons) on the track of Compton electrons traversing the droplets. The acoustic energy distribution of these events coincides with that of events with single nucleation. The peak to the left at small acoustic energy corresponds to noise.

be given of the processes leading to the recorded acoustic signals and the observed α-recoil discrimination. The early theoretical works of Rayleigh [36] and Plesset and Zwick [37] were based on an approximate solution of the Navier–Stokes equation, and postulated that the growth of a vapour bubble in a superheated liquid is controlled by three stages: (i) a surface tension controlled stage, (ii) followed by a stage where the growth is limited by the inertia of the liquid and where the bubble expands with constant velocity, and (iii) an asymptotic stage that is dominated by heat transfer and where the bubble growth is decelerating.

Stage 1. As soon as the bubble radius reaches $R > R_c$, the expansion is driven by the energy stored in the bubble itself and its vicinity. In the initial phase of this stage, the radial velocity of growth is impeded by the effect of the surface tension, but becomes less important with increasing bubble radius.

Stage 2. In the absence of viscous and surface tension effects the subsequent bubble growth is limited by the inertia of the liquid and is described by the Rayleigh–Plesset equation [36]. Its solution implies that the radius increases linearly with time and that the speed of growth is proportional to the square root of the superheat Δp defined in section 2:

$$R_{\mathrm{in}}(t) = A(T) \times t, \quad A(T) = \left(\frac{2}{3\rho_{\mathrm{l}}}\Delta p\right)^{1/2} \tag{10}$$

Since the superheat increases and the liquid density decreases with temperature, the speed of bubble growth also increases with temperature. In particular, we find for C_4F_{10} a prediction of the growth velocity of $A(30\,^{\circ}\mathrm{C}) = 11.6\,\mu\mathrm{m}\,\mu\mathrm{s}^{-1}$ and $A(46\,^{\circ}\mathrm{C}) = 13.6\,\mu\mathrm{m}\,\mu\mathrm{s}^{-1}$.

Stage 3. Due to the expansion of the bubble volume, the vapour within the bubble and also the liquid in the vicinity of the bubble walls cools down until it reaches the boiling temperature

and after a certain characteristic time τ, further growth is only possible if energy is supplied by heat transfer from more and more distant layers of the liquid. From there on, the growth rate becomes limited by thermal diffusion and it decreases continuously. This is described by the Plesset–Zwick equation [37], which in this regime predicts a much slower increase of the bubble radius proportional to the square root of time:

$$R_{\mathrm{th}}(t) = B(T) \times t^{1/2}, \quad B(T) = \left(\frac{12}{\pi}\kappa\rho_{\mathrm{l}}c_{p\mathrm{l}}\right)^{1/2} \frac{T - T_{\mathrm{b}}}{h_{\mathrm{lv}}\rho_{\mathrm{v}}}. \tag{11}$$

Here κ is the thermal conductivity of the liquid and $c_{p\mathrm{l}}$ is its specific heat; the other quantities are as defined in section 2. The growth parameter $B(T)$ can also be expressed as $B(T) = (3\kappa/2\pi)J_a(T)$, where J_a is the Jakob number, a dimensionless quantity that characterizes the speed of bubble growth. In particular, it was found that the $t^{1/2}$ law is only valid for $2 < J_a < 100$ [35, 38]. For C_4F_{10} and within the temperature range considered here, J_a follows a distribution with a broad peak around 35 °C with $J_a = 18.5$ and this decreases slowly and asymmetrically to $J_a = 16.5$ at 20 °C and $J_a = 18$ at 50 °C, respectively. The growth rate 1 μs after nucleation is predicted by (11) to be $\approx 2.5\,\mu\mathrm{m}\,\mu\mathrm{s}^{-1}$, which is already smaller than the speed of inertial growth. The time τ, which is the time at which the transition between the two asymptotic solutions occurs, is strongly model dependent and a scope of investigations [35].

The predictions of growth rates by the classical model are, however, idealizations, and measurements in superheated liquids showed linear growth rates, which were substantially slower than the predicted inertial growth, but still larger than thermal growth up to 100 μs after nucleation [39].

After complete phase transition of a droplet, a freely oscillating vapour bubble is formed. The resulting bubble is a harmonic oscillator, oscillating around its equilibrium radius R_{b} and the ambient equilibrium pressure p_0 with a resonance frequency calculated by Minnaert [40] as

$$\nu_{\mathrm{R}} = \frac{1}{2\pi R_{\mathrm{b}}}\sqrt{\frac{3\kappa p_0}{\rho_{\mathrm{l}}}}, \tag{12}$$

where κ is now the polytropic coefficient of the gas and ρ_{l} the density of the surrounding liquid. For C_4F_{10} at 30 °C the resonance frequency and the bubble radius are related by the simple relation $\nu_{\mathrm{R}}(\mathrm{kHz}) = 2.4/R\,(\mathrm{mm})$. Typical droplets in PICASSO of 100 μm radius will eventually form bubbles of $R_{\mathrm{b}} \approx 0.35$ mm radius and are expected to oscillate with a fundamental frequency of $\nu_{\mathrm{R}} \approx 6$ kHz. This frequency is below the 18 kHz high-pass cut-off used in the analysis of signals discussed in section 9. Moreover, no improvement in the α-recoil discrimination was observed by including frequencies below 10 kHz.

The pressure of the emitted sound, which is produced in the liquid by an expanding or oscillating spherical bubble of radius $R(t)$, is related to the acceleration of its volume V(t):

$$\Delta P(r,t) = \frac{\rho_{\mathrm{l}}}{4\pi}\frac{\ddot{V}(t - r/c)}{r} = \frac{\rho_{\mathrm{l}}}{4\pi r}\left(\frac{4}{3}\pi\right)\frac{\mathrm{d}^2R^3}{\mathrm{d}t^2} = \frac{\rho_{\mathrm{l}}}{r}(2R\dot{R}^2 + R^2\ddot{R}), \tag{13}$$

where $\Delta P(t,r)$ is the pressure change produced in the liquid at a distance r from the source, c is the velocity of sound and ρ_{l} is the density of the liquid [41]. Inserting the solutions for inertial growth $R_{\mathrm{in}}(t)$ and for thermal diffusion-limited growth $R_{\mathrm{th}}(t)$ into (13), one finds the radiated pressure signals for the two modes of asymptotic bubble growth:

$$\Delta P_{\mathrm{in}} \propto \rho_{\mathrm{l}}A(T)^3 \times t \quad \text{and} \quad \Delta P_{\mathrm{th}} \propto \rho_{\mathrm{l}}B(T)^3 \times t^{-1/2}. \tag{14}$$

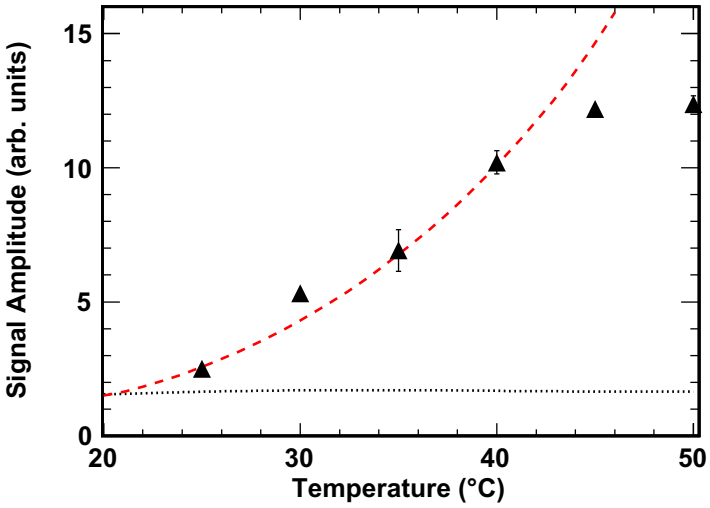

Figure 12. Amplitudes of the measured acoustic signals as a function of temperature compared to theoretical predictions. In the case where bubble growth is driven by thermal diffusion only, the observed signal amplitudes decrease slowly with temperature (dotted); inertial growth predicted by the Rayleigh–Plesset solution of the Navier–Stokes equation predicts a steady rise of the pressure signal with temperature and correspondingly also of the amplitudes (broken). The two theoretical predictions were set to a common value at 20 °C.

Piezoelectric transducers are sensitive to the instantaneous pressure ΔP, with sensitivities quoted in terms of μV μbar^{-1} (section 3). Therefore an analysis of the waveform of the transducer signal allows one to obtain information about the emission process. However, given our present experimental conditions, our timing information is severely limited by the sampling frequency (2.5 μs per sample) and is distorted especially for times larger than 80 μs by reflections and container effects, such as sound propagation in the acrylic. Recent laboratory measurements with sampling frequencies of 1 and 2 MHz indicate an improvement in α-recoil discrimination within the first 50 μs of the waveforms.

Nevertheless, some conclusions about the bubble growth and acoustic signal production can be inferred from the observed amplitudes and their dependence on temperature. Figure 12 compares the measured amplitudes as a function of temperature with those predicted by the two growth models. Apparently only the inertial growth scenario in which the amplitudes increase with temperature shows a trend similar to the data. Since the observed α-recoil discrimination implies a spatial resolution of two nucleation centres separated by about the length of an α-track, i.e. $L_\alpha \sim 40\,\mu$m, it can be concluded that the inertial phase cannot last much longer than about $2L_\alpha/A(T)$: if inertial growth would continue beyond that time, the expanding bubble volumes would have merged completely and all information about multiple nucleation sites would have been washed out. Therefore, after that time, i.e. $t \geqslant 10\,\mu$s, and according to the above estimates for $A(T)$, the decelerating thermal growth phase must have become the dominant effect in order to preserve the information about the spatial extension of the original nucleation volume.

At the moment our α-recoil discrimination data indicate the presence of two to three nucleation centres. However, within the scenario discussed above one would expect that with a better timing resolution of the acoustic read-out system, more nucleation centres or an extended

nucleation region could be resolved along the α-track at an earlier stage of formation, which would result in further improvement of the α-recoil discrimination.

11. Conclusions

The full sensitivity of superheated liquids to nuclear recoils in the absence of a significant sensitivity to γ-rays or minimum ionizing particles has stimulated interest in this technique for dosimetry, neutron detection in fusion research and recently, large-scale applications in dark matter searches. However, some grey areas exist in the detailed understanding of the underlying radiation detection processes: how precisely does radiation induce phase transitions at the nanometer scale, what are the precise dynamics of bubble growth and what time scales are involved, how are the observed acoustic signals produced, and how much information about the nature of the primary event do they contain?

Our recent studies were able to consolidate some known features and to shed new light on some of the open questions: (i) the energy thresholds predicted by the classic nucleation theory in C_4F_{10} are in good agreement with neutron and α-calibration data; only at the lowest neutron energy at 4.8 keV does a discrepancy exist which needs to be clarified; (ii) threshold measurements with detectors spiked with α-emitters allow one to differentiate between energy depositions by the recoiling nuclei and those caused by the Bragg peak of α-particles; (iii) recoil nuclei following α-decay have a higher energy threshold than α-particles; (iv) signals produced simultaneously by recoil nuclei and α-particles have more acoustic energy than signals produced by one or the other separately; (v) neutron and α-data deliver a consistent picture of how the critical interaction length L_c evolves in terms of the critical radius R_c and with temperature; (vi) signal amplitudes increase with temperature, which implies that inertial bubble growth contributes to acoustic signal formation; (vii) the observed α-recoil discrimination requires fine-tuning of the interplay between the inertial bubble growth mode and the asymptotic thermal growth. While our understanding of this interplay is rudimentary at this stage, it is expected that for events occurring entirely in the bulk of the liquid, better discrimination between particle species can be achieved by adapting the speed of the acoustic read-out chain to the timescale that carries most of the information about the primary nucleation process.

Acknowledgments

We acknowledge financial support from the National Sciences and Engineering Research Council of Canada (NSERC), the Canada Foundation for Innovation (CFI) and the Czech Ministry of Education, Youth and Sports. This work was also supported by NSF grant no. PHY-0856273. We thank Andrea Vollrath, Andrea Palenchar and Brendan Sweeney at IUSB for their contributions. We especially thank SNOLAB and its staff for their hospitality and for providing help and competent advice whenever needed.

References

[1] Glaser D A 1952 *Phys. Rev.* **87** 665
[2] Zacek V 1994 *Nuovo Cimento* A **107** 1247
[3] Ing H *et al* 1997 *Radiat. Meas.* **27** 1
[4] Apfel R 1979 *Nucl. Instrum. Methods* **162** 603

[5] Archambault S *et al* (PICASSO Collaboration) 2009 *Phys. Lett.* B **682** 185–92
[6] Aubin F *et al* (PICASSO Collaboration) 2008 *New J. Phys.* **10** 103017
[7] Giroux G 2008 Analyse des données et étude systématique de la réponse des détecteurs dans le cadre du projet PICASSO *MSc Thesis* Université de Montréal
[8] Nadeau P 2009 Alpha-neutron discrimination and droplet size measurements in the PICASSO experiment *MSc Thesis* Laurentian University
[9] Behnke E *et al* 2010 arXiv:1008.3518 [astro-ph.CO]
[10] Felizardo M *et al* 2010 *Phys. Rev. Lett.* **105** 211301
[11] Seitz F 1958 *Phys. Fluids* **1** 2
[12] Harper M J and Rich J C 1993 *Nucl. Instrum. Methods* A **336** 220
[13] d'Errico F 1999 *Radiat. Prot. Dosim.* **84** 55
[14] Norman A and Spiegler P 1963 *Nucl. Sci. Eng.* **16** 213
[15] Poesposoetlipto F and Hugentobler E 1970 *Helv. Phys. Acta* **43** 203
[16] Das M and Sawamura T 2004 *Nucl. Instrum. Methods* A **531** 578
[17] Das M and Sawamura T 2005 *Nucl. Instrum. Methods* A **536** 123
[18] Barnabé-Heider M *et al* 2005 (PICASSO Collaboration) *Nucl. Instrum. Methods* A **555** 184
[19] Behnke E *et al* 2008 *Science* **319** 933
[20] National Institute for Standards and Technology http://webbook.nist.gov/
[21] SRIM J Ziegler http://www.srim.org/
[22] Aubin F 2007 Caractérisation spatiale des événements dans le détecteur PICASSO *MSc Thesis* Université de Montréal
[23] Hahn B 1961 *Il Nuovo Cimento* **22** 650
[24] Gibbons J H, Macklin R L and Schmitt H W 1955 *Phys. Rev.* **100** 167
[25] Auger M 2008 Caractérisation de la réponse des détecteurs aux neutrons de très basses énergies dans PICASSO *MSc Thesis* Université de Montréal
[26] Genest M-H 2007 Recherche du neutralino avec les détecteurs ATLAS et PICASSO *PhD Thesis* Université de Montréal
[27] Lévy C 2009 Gamma calibration using a new test apparatus at Queen's University and optimization analyses for the PICASSO experiment *MSc Thesis* Queen's University
[28] Gornea R 2008 Détection de la matière sombre avec le détecteur àgouttelettes surchauffées dans le cadre du projet PICASSO *PhD Thesis* Université de Montréal
[29] Faust R 2008 Études Monte Carlo des mesures d'étalonnage aux neutrons et aux particules alpha dans PICASSO *MSc Thesis* Université de Montréal
[30] Askaryan G A *et al* 1979 *Nucl. Instrum. Methods* **164** 267
[31] ANTARES http://antares.in2p3.fr
[32] ICECUBE http://icecube.wisc.edu
[33] Martynyuk Y N and Smirnova N S 1991 *Sov. Phys. Acoust.* **37** 76
[34] Archambault S 2010 Discrimination d'événements par analyse des signaux enregistrés par le projet PICASSO *MSc Thesis* Université de Montréal
[35] Robinson A J and Judd R L 2004 *Int. J. Heat Mass Trans.* **47** 5101
[36] Rayleigh L 1917 *Phil. Mag.* **34** 94
[37] Plesset M S and Zwick S A 1954 *J. Appl. Phys.* **25** 493
[38] Cole R and Shulman H L 1966 *Int. J. Heat Mass Trans.* **9** 1377
[39] Shepherd J E 1981 Dynamics of vapor explosions: rapid evaporation and instability of butane droplets exploding at the superheat limit *PhD Thesis* California Institute of Technology
[40] Minnaert M 1933 *Phil. Mag.* **16** 235
[41] Landau L D and Lifschitz E M *Fluid Mechanics* vol VI (Oxford: Butterworth-Heinemann)